J. Fluid Mech. (1997), *vol.* 343, *pp.* 29–41. Printed in the United Kingdom

© 1997 Cambridge University Press

A radioscopic technique to study convective fluid dynamics in opaque liquid metals

By J. N. KOSTER, T. SEIDEL AND R. DEREBAIL†

University of Colorado, Department of Aerospace Engineering Sciences, Boulder, CO 80309-0429, USA

(Received 23 August 1995 and in revised form 2 December 1996)

Experimental verification of theoretical investigations into the behaviour of liquid metal convective flows is required to validate analytical models and numerical simulation codes. A real-time radioscopic density visualization system has been developed and is beginning to provide useful data. The X-ray facility for studying opaque low-Prandtl-number fluid flow is described. Density changes as low as 10^{-3} g cm^{-3} can be visualized by careful control of scatter radiation. The new capability is demonstrated with natural convection benchmark experiments in a narrow vertical layer of gallium melt of aspect ratio $A = 1.4$. The density field in that cell is three-dimensional. Good agreement between calculations and experiments is obtained. Experiments with solidification are provided for further theoretical use.

1. Introduction

The quantitative study of liquid metal fluid dynamics is timely and required to better understand the physics of convective flow and heat transfer in materials and energy science applications (Bergman & Keller 1988; Carpenter & Homsy 1989; Hurle, Jakeman & Wheeler 1983; Ostrach 1983; Szekely & Chhabra 1970). Owing to the lack of experimental flow visualization techniques, the studies have been primarily theoretical with some model experiments involving transparent high-Prandtl-number liquids. However, the driving mechanisms for convective flow in low- and high-Prandtl-number fluids are different, as thermal and viscous boundary layers are different. This difference is expressed by the Prandtl number itself which is a measure of the relative thickness of viscous and thermal boundary layers.

Opaque liquid metals have been probed with thermocouples, electromagnetic techniques, and observations of surface motion (Ricou & Vives 1982; Hart 1983; Camel, Tison & Favier 1986). Stewart & Weinberg (1969, 1971) introduced radioactive tracer materials in liquid tin for visualization purposes. Radioscopy has been employed with much success to non-invasively visualize the morphology of melting and solidification interfaces (Barber *et al.* 1986; Kakimoto *et al.* 1988*a*, *b*; Kakimoto, Eguchi & Hibiya 1991). Kakimoto *et al.* (1988*a*, *b*) used radioscopy with 2.5 mm diameter tracer particles to observe three-dimensional particle movement in molten silicon during crystal growth. Kaukler & Rosenberger (1994) developed radioscopic real time observation of morphological features and particle–interface interactions in Al–1.5 Pb alloys. First efforts to detect diffusion boundary layers in indium-doped silicon during Czochralski crystal growth were presented by Kakimoto *et al.* (1990, 1991).

† Currently with Hewlett Packard Co, San Jose, CA 95131, USA.

https://doi.org/10.1017/S0022112097005909 Published online by Cambridge University Press

Campbell & Koster (1994, 1995) studied natural convection with solidification in a rectangular box and the solidification of InSb in a vertical Bridgman–Stockbarger ampoule which required absorption compensation for the cylindrical geometry. The work showed that the 3.2% density difference between solid and liquid gallium could be clearly visualized with the appropriate image processing techniques. Pool & Koster (1994) showed the potential for density field visualization in convecting and solidifying layers of gallium with a resolution of about $\Delta\rho/\rho = 0.2\%$. This paper reports on further improvements of the visualization of solidification fronts and density profiles in liquid metals subject to natural convection. Improvements were obtained primarily by careful scatter control. The radioscopic technique was tested with a natural convection benchmark study: visualization of isodensity profiles in convecting monocomponent liquid gallium. As the gallium is pure, the isodensity profiles also represent isotherms.

2. Experimental set-up

The natural convection apparatus is inserted into the X-ray beam between the source and the screen. In this experiment, a Plexiglas test cell with a rectangular liquid metal test volume of $50 \times 2 \times 35$ mm^3 was used (figure 1) where the visualization area had the aspect ratio $A = L/H = 50/35 = 1.43$. The fluid is pure gallium (Ga). Heating and cooling of the endwalls was accomplished via molybdenum-cladded copper thermodes. Molybdenum is required to avoid corrosion of the copper thermodes. The hot- and cold-side temperatures were controlled by two precision recirculation thermostats which achieve a short-term temperature constancy of ± 0.1 °C. The large masses of the thermodes improve this temperature constancy. The variation of temperature along the solid–liquid interface of the thermodes was not measured during convection. Design details of the thermodes were favourable to a high homogeneity of the endwall temperature. These details are as follows (cf. tables 1 and 2).

(i) The thin, 0.5 mm, molybdenum plate acts as a thermal barrier between copper and gallium. The thermal conductivity of molybdenum (Mo) is about four times higher than for gallium. Hence, the pertinent temperatures were measured at the Mo foil in the liquid.

(ii) The width of the gallium layer, 2 mm, is much less than the width of the copper thermodes (10 mm).

(iii) Copper has a thermal conductivity which is 14 times higher than gallium. Derebail & Koster (1997) performed calculations on convective flow in the pertinent cavity, and results emphasized the need to include the thermal conductivities of sidewall material, especially the molybdenum foil, in these simulations to match experiments the closest. It is justified to assume that, at least at small temperature differences and with weak convection, isothermal temperatures were achieved in the copper at the interface with the molybdenum foil. The top, bottom, and side walls are thermally insulated with radiographically transparent Plexiglas and additional plastic insulation.

With a computer-controlled data acquisition system and K-type thermocouples, a relative temperature measurement accuracy of ± 0.05 °C and an absolute precision of ± 0.3 °C was achieved. At several locations along the top of the melt, temperature measurements are made with thermocouples (0.5 mm diameter) inserted through holes in the test cell lid. Measurements were also made in the two upper hot and cold corners of the melt to minimize interference with convective flow.

https://doi.org/10.1017/S0022112097005909 Published online by Cambridge University Press

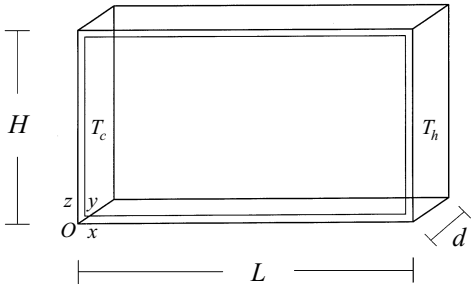


FIGURE 1. Three-dimensional liquid volume. Lead frame sketched at front side.

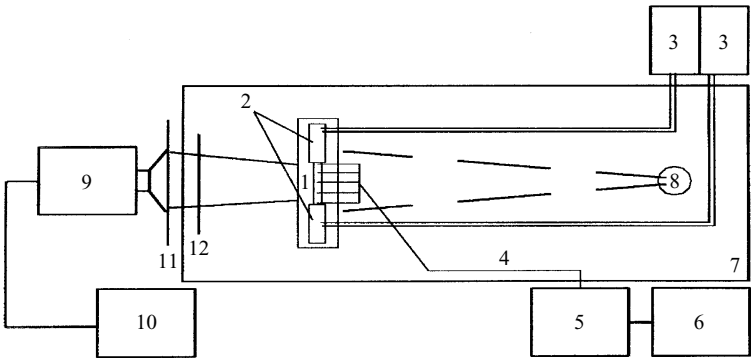


FIGURE 2. Schematic of radioscopy set-up: 1, test cell with liquid metal; 2, thermodes; 3, waterbath temperature control; 4, thermocouples; 5, temperature data acquisition system; 6, PC1; 7, lead chamber; 8, X-ray source; 9, CCD and image processor; 10, PC2; 11, caesium–iodide screen; 12, lead grid.

3. Visualization principle

The experimental facility consists of a conventional non-destructive testing X-ray system and an imaging system (figure 2). The X-ray system includes a continuous, 160 kVp tungsten-target X-ray source which has a spot size of 0.4×0.4 mm². The X-rays are projected onto a caesium–iodide (CsI) fluoroscopic screen, transformed into visible light and recorded via a 30 f.p.s. CCD camera. The video image is then transferred to a computer-controlled image processor. Selected images are transferred to a computer for image postprocessing, such as enhancement and colour coding.

The X-ray beam originating from the tungsten source proceeds in a straight 4° conical volume, and penetrates the test cell before hitting the CsI image intensifier input screen. The intensity of transmitted radiation provides information on the nature of the material and its thickness. When defining the thickness $d = \text{constant}$, the radioscopic image is a shadowgraph picture of the density distribution in the sample melt or solid: the darker regions represent the less penetrable areas (higher density).

The governing equation for X-ray absorption in a particular material is given by

$$I = I_0 \, \mathrm{e}^{-(\mu/\rho)_0 \rho d}, \tag{1}$$

where $(\mu/\rho)_0$ is the reference mass attenuation coefficient, ρ the fluid density, and d the material thickness in the direction of the penetrating radiation (Klug & Alexander 1962). Reference mass attenuation coefficients are tabulated in manuals such as the CRC *Handbook of Physical and Chemical Properties*, or McIntire (1985).

In order to visualize the density of the liquid metal efficiently the material thickness d has to be known precisely, and the X-radiation absorption of the container material

https://doi.org/10.1017/S0022112097005909 Published online by Cambridge University Press

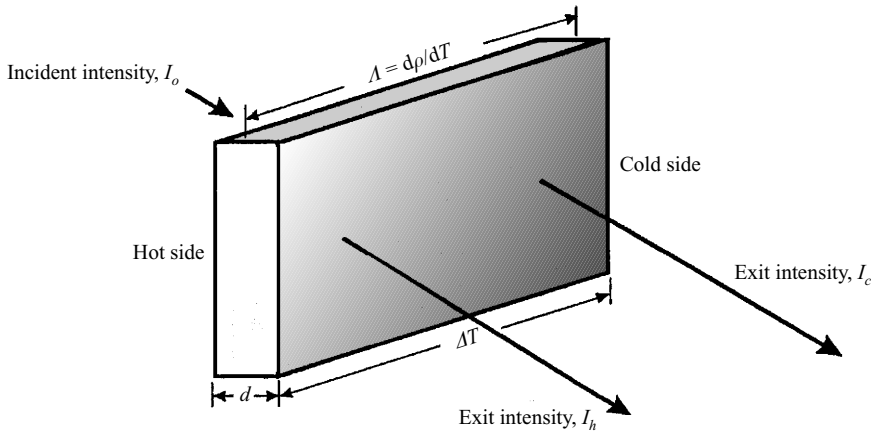


FIGURE 3. Model of exit radiation intensity as a function of the density change in the liquid metal due to an applied temperature difference: $I_c/I_h = \exp[(\mu/\rho)_0 (\Lambda \Delta T)\, d]$.

has to be low, which means that the container material must have a low reference linear absorption coefficient. Plexiglas, a hydrogen–carbon–oxygen-based compound, and the insulating plastic used in our experiments have, in a first approximation, negligible radiation absorption ($(\mu/\rho)_0$ of Plexiglas is 10 times less than for gallium, and gallium is about 10 times more dense). Also, very little, or negligible scatter radiation is generated by Plexiglas. Then, owing to the applied background subtraction method only changes are visualized, with no measurable contribution from the Plexiglas.

It was shown by Pool & Koster (1994) that the difference in absorption from differentially heated opaque liquids provides sufficient variation in intensity levels to be detected by the radioscopic image acquisition system and thus provides density visualization. Given a differentially heated rectangular cavity (figure 3) with a beam path associated with the subscript h (e.g. hot side), and a second beam path associated with the subscript c (e.g. cold side), and assuming that the cavity thickness and mass absorption coefficient are constant on both sides, the ratio of the transmitted intensities from the cold side to the hot side becomes

$$I_c/I_h = \mathrm{e}^{(\mu/\rho)_0 (\Lambda \Delta T)\, d}. \tag{2}$$

Here, the temperature dependence $\Lambda = (-\Delta\rho/\Delta T)$ of a material with $\Delta\rho = \rho_c - \rho_h$ is introduced. For gallium, Λ is given as $\Lambda = 0.56 \times 10^{-3}$ g cm^{-3} K^{-1} (Iida & Guthrie 1988). The variable Λ is assumed constant in the experimental temperature range considered.

Equation (2) implies that the method is an integrating density measurement, over the gap width d, similar to interferometric techniques. Owing to the small variation in density $\rho(T)$ of most liquid metals, the cavity width d in the radiation path has to be precision machined. Any major non-uniformity of the liquid metal thickness will be visualized according to (2), as the product (Λd) would vary locally and thus disturb the anticipated density visualization. The tolerance of the gap width d over the area $H \times L$ was stringent and chosen as $d = 2 \pm 0.05$ mm. Image processing with background subtraction then eliminates residual gap width fluctuations and density changes in the melt are visualized.

It is the intensity variation of the undeviated radiation beam from the specimen which provides useful information for density visualization. The deviated (scattered) radiation leads to mottle and reduces the resolution in density variation visualization,

https://doi.org/10.1017/S0022112097005909 Published online by Cambridge University Press

if not controlled. Any random scatter radiation that hits the CsI screen would reduce the image quality and thus has to be avoided. Sources of noise are the scattered radiation from the lead chamber, from the test apparatus, and from within the melt itself. Mottle is a time-dependent graininess (speckle) in the intensity picture that forms at the CsI screen. This mottle can be controlled to some degree by image processing (see below). A small degree of image blur is created when the X-ray target has a finite size. Blur is caused by the grey halo around the projected shadow of an object which is created by a large-area radiation source. The smaller the target size, the lower the degree of blur (McIntire 1985). The 0.4×0.4 mm^2 spot size of the source leads to a real-time spatial resolution of about ± 0.2 mm for linear objects like the solid–liquid interface. When the image is processed by smoothing, the spatial resolution deteriorates, all depending on the degree of smoothing. Other parameters which can affect image clarity (such as the distance from the liquid layer to the imaging screen, and the distance from the liquid layer to the X-ray source) have to be optimized to within the physical limitations of the facility. Radiation path concerns will be addressed in the next section.

The environmental scatter from all metallic parts in the experiment set-up is greatly reduced by careful lead masking. Pure, so-called 'virgin' lead is preferred for near-perfect radiation absorption. The CsI screen is covered by lead shutters which are opened only to the cross-sectional area needed. This masking limits stray radiation from the X-ray chamber. One of the first improvements made was to design a beam-limiting aperture, a lead diaphragm (often inaccurately called 'collimator'), which limits the conical X-ray beam to the size of the liquid layer to be studied. This device reduces the radiation that reaches the radiographic chamber wall (and other equipment) to generate scatter from the environment.

The conical radiation beam entails a major drawback: some of the area of interest (liquid layer) has to be covered in order to avoid Bragg scatter at the sidewalls. The window opening is chosen so as to eliminate grazing-incidence Bragg-scatter generation at the molybdenum-lined copper thermodes. This means that in figures 4, 5 and 6, below, the actual cavity extends about 1 mm beyond the visualized area, and information directly at the endwalls is therefore lost.

After all this masking, the only generation of scatter left is in the liquid metal itself. To limit this scatter we use a focused criss-cross lead grid with 40 lines cm^{-1} and a grid aspect ratio 8:1. A focused criss-cross grid is composed of two lead grids with a focal range of 90 ± 5 cm, such that the conical X-ray source beams are about parallel to the lead strips in the grid. The purpose of the grid is to allow the straight X-rays that originate at the X-ray source to pass through. Finally, some scatter is generated by the CsI-screen itself (scintillation noise level), which is considered a technological limitation, and fortunately less important than Bragg-scatter from the equipment.

With these efforts of scatter control, an unprecedented quality of density visualization was achieved. This improvement in the quality of the original visualization image is required before electronic image processing can be applied. The image processing is described next.

A significant effort goes into image processing. The visible light image created by the image intensifier after the CsI-screen is captured by a high-resolution CCD camera ($768(H) \times 493(V)$ pixel resolution). Recursive filtering (comparison of two consecutive output images to the current input image according to $V_n = V_{n-1} + (V_{in} - V_{n-1})/N$, where V_n = output image, V_{n-1} = output image for previous frame, V_{in} = input image, $N = 2, 4, 8, \ldots, 128$) is applied to the images first. Real-time background image subtraction provided a means to get rid of systematic irregularities in the radiation

https://doi.org/10.1017/S0022112097005909 Published online by Cambridge University Press

path and to show only changes in the intensity distribution (the background image serves a similar function as the hologram in holographic real-time interferometry). The isothermal state of the liquid gallium provides a suitable background image. When a temperature gradient is applied and the background image is subtracted from the real-time image, the resulting image consists of information on the changes in the intensity field. These intensity changes are correlated to density changes (equation (2)). The image processor performs electronic contrast enhancement by adjusting the electronic gamma-curve (output grey scale versus input grey scale) in the LUT (Look Up Tables). These LUT include functions for changing (linearly or nonlinearly) output values corresponding to specific input values, which involves setting the intensity levels of the black and white colours and the 254 grey levels in between, as various step functions, or as alternating black and white fringes to show patterns similar to interference fringes in interferometry.

4. Mathematical model and numerical simulation

In order to benchmark the visualization experiments, we modelled the natural convection in monocomponent gallium (table 1). The flow field and temperature distribution are governed by the steady-state three-dimensional Navier–Stokes and energy equations.

The steady-state governing equations were non-dimensionalized (denoted by *) using the following dimensional variables:

$$\left.\begin{aligned} &x^* = x/H, \quad y^* = y/H, \quad z^* = z/H, \\ &u^* = \frac{u}{(\kappa/H)}, \quad v^* = \frac{v}{(\kappa/H)}, \quad w^* = \frac{w}{(\kappa/H)}, \\ &p^* = \frac{p}{\rho(\kappa/H)^2}, \quad T^* = \frac{T-T_c}{T_h-T_c}, \end{aligned}\right\} \tag{3}$$

where x, y, z are the distances in the x-, y- and z-directions; u, v, w the velocities in the x, y, z directions; H is the height of the cavity, p the hydrodynamic pressure, T_c and T_h the temperatures at the cold and hot walls, respectively, ρ the density, and κ the thermal diffusivity of the melt.

The dimensionless governing equations of conservation of mass, momentum and energy (after eliminating the *) are written as

$$\boldsymbol{\nabla}\cdot\boldsymbol{u} = 0, \tag{4}$$

$$(\boldsymbol{u}\cdot\boldsymbol{\nabla}\boldsymbol{u}) = -\boldsymbol{\nabla}p + Pr\,\nabla^2\boldsymbol{u} + A\,Ra\,Pr\,T\boldsymbol{e}_z, \tag{5}$$

$$\boldsymbol{u}\cdot\boldsymbol{\nabla}T = \nabla^2 T, \tag{6}$$

where $\boldsymbol{u}$ is the velocity vector ($\boldsymbol{u} = \{u, v, w\}$, $A = L/H$, the aspect ratio of the cavity, $\boldsymbol{e}_z$ the vertical unit vector in the negative z-coordinate, Ra the Rayleigh number, and Pr the Prandtl number.

The Grashof number, Gr, the Prandtl number, Pr, and the Rayleigh number, Ra, are defined as follows:

$$Gr = \frac{g\beta[(T_h - T_c)/L]H^4}{\upsilon^2}, \tag{7}$$

$$Pr = \upsilon/\kappa, \tag{8}$$

$$Ra = Gr\,Pr, \tag{9}$$

https://doi.org/10.1017/S0022112097005909 Published online by Cambridge University Press

Parameter	Symbol	Value	Units	References
Melting point	T_m	29.78	°C	[1]
Volumetric coefficient of thermal expansion (373 K)	β	1.2×10^{-4}	K^{-1}	[1]
Viscosity	μ	2.04×10^{-3}	kg m^{-1} s^{-1}	[2]
Density (302.78 K)	ρ	6094.70	kg m^{-3}	[1]
Momentum diffusivity	ν	3.347×10^{-7}	m^2 s^{-1}	calc.
Thermal conductivity (302.78 K)	k	28.68	W m^{-1} K^{-1}	[1]
Specific heat (500 K)	c_p	384.7	J kg^{-1} K^{-1}	[2]
Thermal diffusivity	κ	1.223×10^{-5}	m^2 s^{-1}	calc.
Prandtl number	Pr	0.023	1	calc.

TABLE 1. Parameters for gallium, [1] *Metals Handbook*, *Tenth Edn*, Vol. 2, *Properties and Selection: Nonferrous Alloys and Special-Purpose Materials*, ASM International 1990, pp. 1114–1115; [2] *Metals Handbook*, Desk Edition, ASM (1984), pp. 2–19.

Parameter	Symbol	Value	Units	Reference
	Plexiglas			
Thermal conductivity (293 K)	k	0.20	W $(m\ K)^{-1}$	[1]
Specific heat	c_p	1466	J $(kg\ K)^{-1}$	[1]
	Molybdenum			
Thermal conductivity (298.2 K)	k	138	W $(m\ K)^{-1}$	[2]
Specific heat (298 K)	c_p	250	J $(kg\ K)^{-1}$	[2]
	Copper			
Thermal conductivity (298.2 K)	k	401	W $(m\ K)^{-1}$	[2]
Specific heat (298 K)	c_p	384	J $(kg\ K)^{-1}$	[2]

TABLE 2. Parameters for solid wall materials. [1] *DUPONT Polymer Products*, Lucite® Acrylic data sheet; [2] *Handbook of Chemistry and Physics*, 70th Edn, 1989–1990, CRC Press.

where ν is the kinematic viscosity, g the acceleration due to gravity, and β the coefficient of thermal expansion. All fluid properties are constant except for the density appearing in the body force term in (5) where $\rho(T)=\rho_0(1-\beta\Delta T)$.

The Plexiglas walls and the molybdenum walls are a solid entity within the model, and therefore the energy equation must be solved in the walls:

$$\kappa^s\nabla^2 T=0, \tag{10}$$

where κ^s is the thermal diffusivity of the solid (either Plexiglas or Mo, respectively).

No-slip boundary conditions are imposed at the top, bottom, front and back rigid walls. These walls have finite thermal conductivity properties (table 2). Outside the Plexiglas walls, the thermal boundary condition is set to adiabatic. Outside the heated 0.5 mm thick molybdenum plates at the copper thermodes (heated and cooled walls), the thermal boundary conditions are set to perfectly conducting:

$$\left.\begin{aligned}&\boldsymbol{u}=0,\quad T=T_c\quad\text{at}\quad x=-0.5\text{ mm}\quad\forall y,\forall z;\\&\boldsymbol{u}=0,\quad T=T_h\quad\text{at}\quad x=L+0.5\text{ mm}\quad\forall y,\forall z,\end{aligned}\right\} \tag{11}$$

Perfect thermal contact is assumed at the melt/molybdenum interface and the melt/Plexiglas interface, so that the conductive fluxes at this boundary are equal. From the general heat transfer equation

$$q=-k\,\mathrm{d}T/\mathrm{d}x, \tag{12}$$

https://doi.org/10.1017/S0022112097005909 Published online by Cambridge University Press

with the heat conductivity k, we equate the thermal fluxes between melt (m) and solid (s) in non-dimensional form as

$$q^m = q^s \tag{13}$$

or $\nabla T^m = \gamma \nabla T^s$, where $\gamma = k^s/k^m$ is the ratio of the thermal conductivities of the solid wall material to that of the gallium melt.

A limitation in the computation of the Grashof number is that the temperature at the molybdenum–gallium interface is not known precisely; thermocouples just touch the Mo-plate. The assumption of a perfectly conducting boundary condition as used in numerical modelling is valid at the copper surface behind the molybdenum foil (Derebail & Koster 1997).

The flow is assumed to be steady, laminar, incompressible and three-dimensional. The nonlinear governing equations were discretized and solved numerically by using the finite element code FIDAP (Release 7.51). FIDAP uses the conventional finite element Galerkin formulation.

Eight-node continuum brick elements were employed for the discretization of temperature and velocity. A graded mesh with $59 \times 23 \times 55$ grid points in the x-, y- and z-directions was employed to include solid walls and the liquid layer. The liquid layer itself is covered by $50 \times 11 \times 40$ grid points in the x-, y- and z-directions ($50 \times 2 \times 25$ mm^3 liquid volume). Grid tests led to the conclusion that this particular grid resolution (which approaches the limits of our computer resources) is sufficient for the accuracy of the solutions. More details of the numerical modelling, the gridding, and the assessment of the contributions of the walls can be found in Derebail & Koster (1997).

Convergence of the numerical calculations is achieved whenever the following criteria are satisfied:

$$\frac{\|\boldsymbol{u}_i - \boldsymbol{u}_{i-1}\|}{\|\boldsymbol{u}_{i-1}\|} \leqslant 10^{-3}, \tag{14}$$

$$\frac{\|R(\boldsymbol{u}_i)\|}{\|R_0\|} \leqslant 10^{-3}, \tag{15}$$

where $\|\cdot\|$ is the Euclidean norm, $\boldsymbol{u}_i$ is the solution vector, and $R(\boldsymbol{u}_i)$ is the residual vector (i indicates the ith iteration). Because both $\nabla \boldsymbol{u}_i$ and $R(\boldsymbol{u})$ tend to zero near the real solution, a combination of these two criteria provides a sufficient and effective overall convergence criterion for all possible situations.

The solution strategy for this three-dimensional problem was to perform one or two iterations with the *Successive Substitution Solution* algorithm and then switch to the *Segregated Solver* solution algorithm. The strategy of using the slower but more robust successive substitution method in the early phase of calculations was to bring the solution within the radius of convergence of the faster-converging segregated solver method.

5. Results on natural convection in pure gallium

The objective of this study was to develop the flow visualization technique for opaque liquid metals. As a benchmark case, we consider natural convection in liquid gallium. Thermophysical data of the 99.99 % pure gallium (Ga) are given in table 1. Its melting point is $T_m = 29.8$ °C. Initially, the melt and test cell are kept isothermal at a temperature of about 35 °C for a minimum of three hours or overnight. The thermal diffusion time in the gallium confined in our test cell is $\tau = L^2/(\kappa) = 204$ s (where κ is the thermal diffusivity of gallium), and in the Plexiglas it is $\tau = 22$ min. Thermodynamic equilibrium was thus guaranteed after one hour at constant temperature levels. This

https://doi.org/10.1017/S0022112097005909 Published online by Cambridge University Press

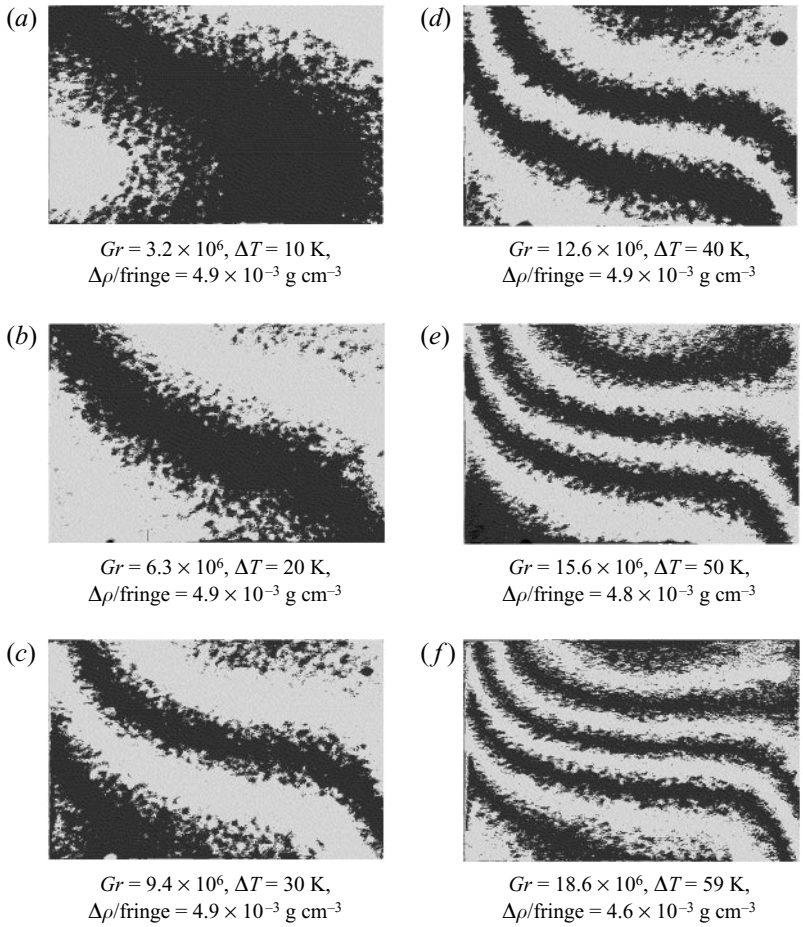


FIGURE 4. Radioscopic density/temperature field visualization of natural convection in liquid gallium ($Pr = 0.023$). Left-hand side is at T_c, right-hand side is at T_h.

uniform density distribution in the melt with equal X-ray absorption provided the electronic background image. Differential heating from the side was applied for a limited time with a ramping rate of 0.3 K min^{-1}. Each plateau of constant temperature difference is given a thermal equilibration time of at least one hour. Temperature difference values for the Grashof number calculation were taken from the thermocouples located in the top corners of the cavity, protruding 2 mm into the melt and in contact with the thermodes. For the determination of the Grashof number in the case that included solidification, the cold temperature was defined as $T_c = T_m$, the melting temperature of Ga. The distance between the hot wall and the interface at the top boundary of the melt was taken as the characteristic length.

Visualization results are shown in figure 4. The right-hand side of each picture is the heated side and the left-hand side is the cooled side. Natural convection develops at $\Delta T > 0$. The grey scale of the live image was linear. The enhanced linear profile was then changed by the LUT into a homogeneous step function of equal step heights and width (stairs). The number of steps (called 'fringes' in interferometry) was chosen arbitrarily such that the resolution at small temperature difference is sufficient (e.g. 3 fringes), and at high temperature the image is still readable (e.g. 10 fringes). Each

https://doi.org/10.1017/S0022112097005909 Published online by Cambridge University Press

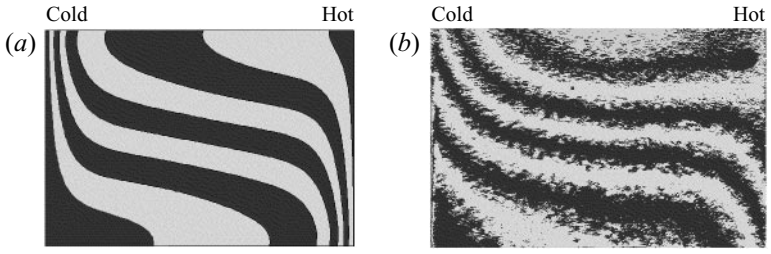


FIGURE 5. (*a*) Numerically simulated temperature distribution in liquid gallium at $\Delta T = 60$ K and $Gr = 1.86 \times 10^7$. Each image has nine fringes to show the same $\Delta\rho/\text{fringe} = 4.6 \times 10^{-3}$ g cm^{-3}. Compare to experiment in figure 4(*f*) reproduced here as (*b*).

fringe (step) was then colour coded alternately in dark and light grey. The density change between two steps (fringes) was calculated from the $\rho(T_h)$, and $\rho(T_c)$ values used for the determination of Gr and the number of steps at the specific Grashof number. The settings in the image processing were calculated to correspond to a density change of $\Delta\rho/\text{fringe} = 0.0049$ g cm^{-3}. This resolution is equivalent to $\Delta\rho/\rho = 0.08\,\%$, a significant improvement over the earlier results by Pool & Koster (1994).

Hot fluid is moving upwards at the right-hand wall and downwards at the cold wall. Owing to the finite conductivity of the sidewalls, the liquid gallium is heated as it moves up, which is visualized as a change in density. The same is valid for the cold side. It should be remembered that owing to the visualization constraints discussed above, a 1 mm liquid frame is excluded from the field of view by a lead frame. This design constraint leads to the visualization of fringes that appear to enter the vertical sidewalls.

As the density change in liquid Ga is rather small, the resolution is limited at low Grashof number ($Gr \leqslant 3.2 \times 10^6$). At higher Gr, the resolution (in terms of fringe number) improves as the density change across the test cell becomes larger. In the centre of the layer a vertical density stratification develops with increasing temperature difference. The experimental work of Stewart & Weinberg (1971), using thermocouple probes, shows similar convective patterns. At very high ΔT the upper density fringe dips somewhat, which may be indicative of an experimental artifact, which we cannot explain at this time. The most likely cause of the dip is the conical X-ray beam and off-centre set-up of the test cell.

In order to evaluate the accuracy of the visualized density fields, we modelled the cavity problem with FIDAP, including finite thermal conductivity of the boundaries (Derebail & Koster 1997). As the experimental signal is integrated through the liquid layer and walls, the calculated temperature field in figure 5 was computed by averaging the temperature values of eleven two-dimensional vertical planes through the liquid layer (the sidewalls are transparent to the radiation and do not affect the visualization). The temperature field was colour coded in grey shades, similarly to the experiments, to facilitate visual comparison with the experiment. Remember that in the experiments a lead window cuts out a framing area of about 1 mm of liquid.

There is still a technology limitation in resolution ($\Delta\rho$/fringe) for the experimental technique when compared to the 'clean' numerical simulations. Nevertheless, the density field patterns of experiments and calculations are considered in good, and state-of-the-art, agreement. The modelling validates our interpretation of fluid physics obtained by the radiographic density visualization. Numerical tests by Derebail & Koster (1997) with fully time-dependent Navier–Stokes equations confirmed the steady-state convection at these Grashof numbers.

https://doi.org/10.1017/S0022112097005909 Published online by Cambridge University Press

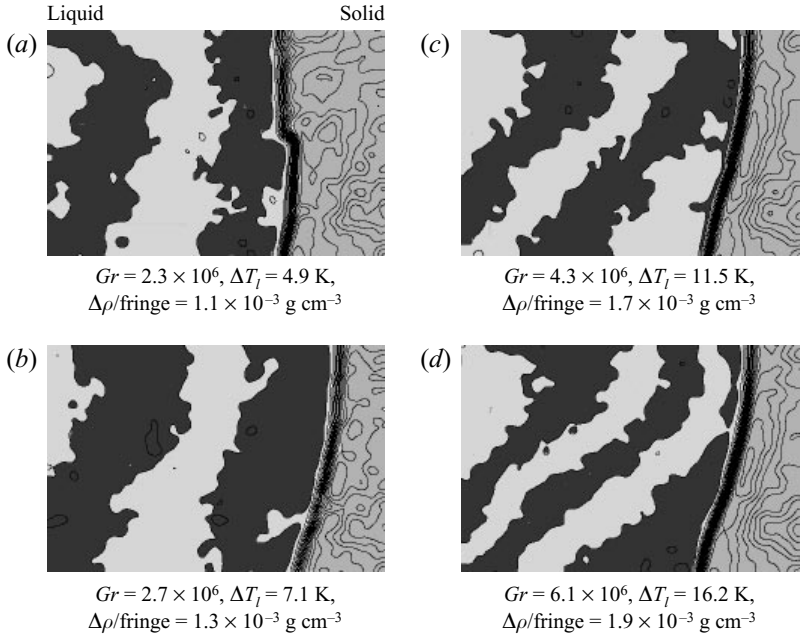


FIGURE 6. Radioscopic temperature field visualization of convective flow in solidifying liquid Ga ($Pr = 0.023$). The left-hand wall is heated. Temperature difference is calculated across the liquid layer.

Additional experiments were performed to include solidification of the pure gallium (figure 6). The objective was to study the density field in the liquid and the influence of steady-state natural convection on the interface morphology. This problem is of major interest in materials science. The experiment procedures were chosen to keep the solid and interface location at the right-hand end of the test cell. The density fields were smoothed in up to 50 passes, the melt was colour-coded, and the solid was coloured medium grey. An unavoidable drawback of the smoothing, which is geared toward getting high-quality density fringes in the melt, is the increased blur of the interface location.

The lighter melt flows upward along the hot sidewall. The colder melt flows downward along the interface. The interface at $Gr = 2.3 \times 10^6$ reveals grain growth of the solid, which is hardly influenced by the natural convective flow. At higher Grashof number ($Gr \geqslant 2.7 \times 10^6$) the natural convection smooths the interface morphology of the grain structure. These flow patterns can be compared to the results presented by Gau & Viskanta (1986), Kuo & Korpela (1988), and Campbell & Koster (1994). The achieved density difference per colour step in the melt was $\Delta\rho$/fringe = 0.0011 g cm^{-3}. This is equivalent to a resolution of $\Delta\rho/\rho = 0.02\,\%$, which is the highest resolution we have achieved so far in pure element melts.

6. Conclusion

Visualization of density fields in convecting monocomponent liquid gallium with a novel radioscopic technique has been demonstrated successfully. As the density in most low-Prandtl-number metallic melts changes only weakly as a function of temperature, efforts are required to push the resolution of the radioscopic system to its limits,

https://doi.org/10.1017/S0022112097005909 Published online by Cambridge University Press

requiring careful control of the radiation environment. The highest resolution achieved in the detection of density change was 0.02%. Results were compared to numerical simulations of the three-dimensional natural convection cavity case and found to be in good agreement, which validates the new experimental technique. Mastering the technology issues related to making a very clean radiation beam led to a powerful new density visualization technique for liquid metal fluid mechanics studies.

The research support from the NSF under CTS-8905846 and CTS-9114775 is greatly appreciated. The study also benefited from NASA support under NCC3-210. We appreciate the valuable discussions with T. Campbell. T.S. thanks the Frankfurter Flughafen Stiftung for financial support for his visit. He also thanks Professor J. Straub for his encouragements and support to do his Diploma-thesis at Colorado.

REFERENCES

Barber, P. G., Crouch, R. K., Fripp, A. L., Debnam, W. J., Berry, R. F. & Simchick, R. 1986 A procedure to visualize the melt-solid interface in Bridgman grown germanium and PbSnTl. *J. Cryst. Growth* **74**, 228–230.

Bergman, T. & Keller, J. 1988 Combined buoyancy, surface tension flow in liquid metals. *Numer. Heat Transfer* **13**, 49–63.

Camel, D., Tison, P. & Favier, J. J. 1986 Marangoni flow regimes in liquid metals. *Acta Astronautica* **13**, 723–726.

Campbell, T. A. & Koster, J. N. 1994 Visualization of liquid/solid interface morphologies in gallium subject to natural convection. *J. Cryst. Growth* **140**, 414–425.

Campbell, T. A. & Koster, J. N. 1995 Radioscopic visualization of indium antimonide growth by vertical Bridgman–Stockbarger technique. *J. Cryst. Growth* **147**, 408–410.

Carpenter, B. M. & Homsy, G. M. 1989 Combined buoyant-thermocapillary flow in a cavity. *J. Fluid Mech.* **207**, 121–132.

Derebail, R. & Koster, J. N. 1997 Numerical simulation of natural convection of gallium in a narrow gap. *Intl J. Heat Mass Transfer* **40**, 1169–1180.

Gau, C. & Viskanta, R. 1986 Melting and solidification of a pure metal on a vertical wall. *Trans. ASME*: *J. Heat Transfer* **108**, 174–181.

Hart, J. 1983 A note on the stability of low-Prandtl-number Hadley circulations. *J. Fluid Mech.* **132**, 271–281.

Hurle, D. T. J., Jakeman, E. & Wheeler, A. A. 1983 Hydrodynamic stability of the melt during solidification of a binary alloy. *Phys. Fluids* **26**, 624–626.

Iida, T. & Guthrie, R. I. L. 1988 *The Physical Properties of Liquid Metals*, p. 71. Clarendon.

Kakimoto, K., Eguchi, M. & Hibiya, T. 1991 In-situ monitoring of dopant concentration variation in a silicon melt during Czochralski growth. *J. Cryst. Growth* **112**, 819–823.

Kakimoto, K., Eguchi, M., Watanabe, H. & Hibiya, T. 1988*a* Direct observation by X-ray radiography of convection of molten silicon in the Czochralski growth method. *J. Cryst. Growth* **88**, 365–370.

Kakimoto, K., Eguchi, M., Watanabe, H. & Hibiya, T. 1988*b* In-situ observation of solid-liquid interface shape by X-ray radiography during silicon single crystal growth. *J. Cryst. Growth* **91**, 509–514.

Kakimoto, K., Eguchi, M., Watanabe, H. & Hibiya, T. 1990 In-situ observation of impurity diffusion boundary layer in silicon Czochralski growth. *J. Cryst. Growth* **99**, 665–669.

Kaukler, W. F. & Rosenberger, F. 1994 X-ray microscopic observations of metal solidification dynamics. *Metall. Mat. Trans.* A **25A**, 1775–1777.

Klug, P. K. & Alexander, L. E. 1962 *X-ray Diffraction Procedures*, pp. 78–103. Wiley.

Kuo, H. P. & Korpela, S. A. 1988 Stability and finite amplitude natural convection in a shallow cavity with insulated top and bottom and heated from the side. *Phys. Fluids* **31**, 33–42.

McIntire, P. (ed.) 1985 *Nondestructive Testing Handbook*; 2nd edn, vol. 3. Radiography and Radiation Testing, American Society for Nondestructive Testing.

https://doi.org/10.1017/S0022112097005909 Published online by Cambridge University Press

Ostrach, S. 1983 Fluid mechanics in crystal growth – the 1982 Freeman Scholar lecture. *Trans. ASME: J. Fluids Engng* **105**, 5–20.

Pool, R. E. & Koster, J. N. 1994 Visualization of density fields in liquid metals. *Intl J. Heat Mass Transfer* **37**, 2583–2587.

Ricou, R. & Vives, C. 1982 Local velocity and mass transfer measurements in molten metals using an incorporated magnet probe. *Intl J. Heat Mass Transfer* **25**, 1579–1588.

Stewart, M. J. & Weinberg, F. 1969 Flow of liquid tin in a square enclosure. *Trans. AIME* **245**, 2108–2110.

Stewart, M. J. & Weinberg, F. 1971 Fluid flow in liquid metals II. Experimental observations. *J. Cryst. Growth* **12**, 228–238.

Szekely, J. & Chhabra, P. S. 1970 The effect of natural convection on the shape and movement of the melt-solid interface in the controlled solidification. *Metall. Trans.* B **1**, 1195–1203.

https://doi.org/10.1017/S0022112097005909 Published online by Cambridge University Press